

Mode Q factor and lasing spectrum controls for deformed square resonator microlasers with circular sides

Hai-Zhong Weng, Yong-Zhen Huang,* Yue-De Yang, Xiu-Wen Ma, Jin-Long Xiao, and Yun Du
State Key Laboratory on Integrated Optoelectronics, Institute of Semiconductors & University of Chinese Academy of Sciences, Chinese Academy of Sciences, Beijing 100083, China

(Received 3 December 2015; revised manuscript received 3 May 2016; published 23 January 2017)

Stable dual-mode lasing semiconductor lasers can be used as a seed source for photonic generation of optical frequency comb and terahertz carrier. Normal square resonator microlasers can support dual-mode lasing with frequency interval up to 100 GHz. Here we demonstrate ultrahigh Q deformed square resonators with the flat sides replaced by circular sides for further increasing transverse mode intervals. The stable condition of dual-mode lasing is verified based on nonlinear gain analysis. Furthermore, the beating signals of 0.43, 0.31, and 0.16 THz are obtained by the autocorrelation measurement, which indicate the deformed microlasers as an architecture for THz radiation generation. The deformed square resonators pave the way for controlling the lasing spectrum and serve as ultrahigh Q microresonators for photonic integrated circuits.

DOI: [10.1103/PhysRevA.95.013833](https://doi.org/10.1103/PhysRevA.95.013833)

I. INTRODUCTION

Optical microresonators that exploit total internal reflection (TIR) of light rays can have high-quality (Q) whispering-gallery modes (WGMs), which are of great importance for fundamental physics studies and practical device applications [1–3]. With the advantages of small mode volume and low power consumption, WGM microlasers such as microdisk lasers are attractive as potential light sources for on-chip optical interconnection and photonic integrated circuits [4,5]. Directional emission microlasers breaking the rotational symmetry and preserving high Q modes were designed by using asymmetrical microcavities [6–9], spiral microcavity [10,11], Limaçon microcavity [12], harmonic series shape microcavity [13–16], and local perturbations of a scatter or a notched ellipse [17–20]. Ultrahigh Q modes in deformed microcavities were demonstrated with channeling chaotic rays into waveguides for efficiently unidirectional output [21]. In addition to microdisk resonators, equilateral-polygonal microcavities can also support high Q WGMs for the applications in microlasers [22–26]. Interestingly, a quasianalytical solution can be given for the WGMs in square microcavities with integrable internal dynamics [22,23]. Square resonator microlasers have been designed for single-mode lasing, dual-mode lasing, and enhancement of mode Q factors [27–31]. Dual-mode lasing with a tunable interval from 30 to 40 GHz was demonstrated for a square microlaser with a patterned electrode and a vertex waveguide [27], and was applied to generate a microwave signal. However, the lasing mode interval is limited by the size of the square microlaser due to the requirement of high passive Q factors for dual-mode lasing. In addition, stable dual-mode lasing requires overcoming mode competition, which is not clear for the square microlasers. To avoid the inevitable mode competition, quantum dot semiconductor lasers were proposed for stable dual-mode lasing [32].

Here, we propose and demonstrate deformed square microlasers with the flat sides replacing by circular sides for controlling lasing mode spectra. By introducing a circular-side

square resonator (CSR), we can modify the lasing mode spectra by greatly enhancing transverse mode intervals and mode Q factors. The circular sides can work as concave mirrors for focusing the mode light beam in the CSRs, which are widely used in conventional gas or solid laser systems but rarely applied to the polygonal microresonators. By varying the radius of the circular side, we can avoid the radiation loss from the vertices of the square resonator and greatly enhance the passive mode Q factors. The ultrahigh passive mode Q factors of the fundamental and first-order transverse modes can result in dual-mode lasing, as they can have near equal mode Q factors accounting for the internal absorption loss. Furthermore, the stability of the dual-mode lasing is verified based on nonlinear gain analysis accounting for mode field distributions for square resonator and CSRs. Dual-mode lasing CSR microlasers are demonstrated with mode intervals in sub-THz range, agreeing well with numerical simulation, which can be applied for photonic generation of sub-THz waves for wireless communication [33,34]. In addition, dual-wavelength lasing microlasers can also be applied as a seed light source for generating optical frequency comb by cascaded four-wave mixing in a nonlinear optical fiber [35–37].

II. MODE CHARACTERISTICS ANALYSIS

A two-dimensional (2D) schematic of the proposed CSR with an output waveguide connected to one vertex is shown in Fig. 1, which is confined by the bisbenzo cyclobutene (BCB). The deformed geometry is realized by replacing the straight boundaries of the square microresonator with circular sides. A deformation amplitude δ is defined by $\delta = r - \sqrt{r^2 - (a/2)^2}$, where a is the flat-side length and r is the radius of the circular side.

The 2D CSRs without waveguides are firstly simulated by the light ray analysis, assuming the effective refractive index n of 3.2 and 1.54 for the resonator and surrounded BCB, respectively. Upper half Poincaré surface of sections with 360 initial polar angles and 2000 bounces are presented in Figs. 2(a)–2(d) for the CSRs with deformation amplitude δ of 0, 0.5, 0.9, and 1.3 μm , respectively, as $a = 16 \mu\text{m}$.

*yzhuang@semi.ac.cn

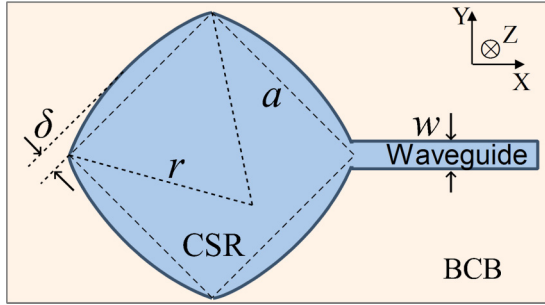


FIG. 1. Schematic diagram of the 2D deformed square microresonator with an output waveguide connected to a vertex.

Light rays are approximately considered to be leakage as they impinge on the vertices. The real ray trajectories trapped by TIR are illustrated in the insets with the starting point at $(\theta, \sin \chi) = (0, 0.73)$ and marked by the red symbols in the phase space. In Fig. 2(a), the horizontal lines in the phase space indicate that the mode light rays impinge on the whole resonator with the complementary incident angles at the adjacent sides. In Fig. 2(b), the intensive closed curves around $\theta = 0, \pi/2, \pi, 3\pi/2,$ and 2π are corresponding to high Q WGMs, surrounded by the external chaotic regions. At $\delta = 0.9 \mu\text{m}$, the ray orbits are scattered randomly with very small islands in Fig. 2(c), but regular triangle-like islands are formed again in Fig. 2(d) at $\delta = 1.3 \mu\text{m}$. These results indicate that the circular arcs can confine the mode light rays away from the vertices of the CSR at $\delta = 0.5$ and $1.3 \mu\text{m}$, which can enhance the mode Q factors and transversal mode intervals and are in good agreement with the following finite-element method (FEM) simulations.

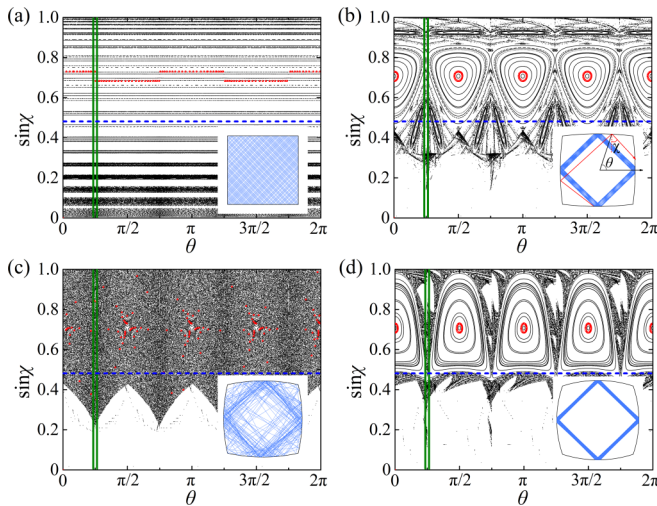


FIG. 2. (a)–(d) Upper Poincaré surface of sections at $a = 16 \mu\text{m}$ and $\delta = 0, 0.5, 0.9,$ and $1.3 \mu\text{m}$, respectively, where θ and χ denote the polar angle of reflection position and incident angle as shown in the inset of (b). The horizontal dashed lines and vertical solid lines indicate the critical angle of the total internal reflection and the exit window into the waveguide, respectively. Insets: The real ray trajectories with 200 bounces inside the CSR with the starting point at $(\theta, \sin \chi) = (0, 0.73)$, corresponding to the red symbols in the phase space.

The mode characteristics of CSRs are then investigated using a 2D FEM. In the simulation, a perfectly matched layer (PML) is used to terminate the calculation region, and the distances between the PML and the resonator edge are larger than $2 \mu\text{m}$. To ensure the accuracy of the numerical calculation, the maximum size of the mesh is $1.5/10n$ (μm) with the refractive index n . The mode characteristics of symmetric transverse electric (TE) modes relative to the middle line of the output waveguide are presented here. For a 2D CSR with $a = 16 \mu\text{m}$ and $w = 1.5 \mu\text{m}$, mode resonance wavelengths and Q factors versus δ are plotted in Figs. 3(a) and 3(b) for the fundamental (zeroth-), first-, and second-order transverse modes. The redshifts of the mode wavelengths are about 17 nm as δ increases $0.1 \mu\text{m}$ for the zeroth-order transverse mode due to the increase of the resonator size. The longitudinal mode numbers are changed with δ to keep the mode wavelength around 1550 nm . So the mode wavelengths marked by open (half-filled) symbols only belong to the same longitudinal mode number at the same value of δ , and the transverse mode intervals gradually increase with δ . The mode Q factors of the zeroth- and first-order transverse modes take the maximum values of 8.7×10^9 and 2.1×10^8 at $\delta = 0.4 \mu\text{m}$, and 1.9×10^{11} and 2.7×10^{10} at $\delta = 1.4 \mu\text{m}$, respectively. And the mode Q factors take the minimum values at about $\delta = 0.95 \mu\text{m}$, as predicted by the light ray simulation.

The distributions of $|H_z|$ are plotted in Figs. 4(a)–4(d) at $\delta = 0, 0.5, 0.9,$ and $1.3 \mu\text{m}$ for the zeroth- and first-order transverse modes, respectively. The high Q mode field patterns in Figs. 4(b) and 4(d) have narrow transverse field distributions with near constant width and flat phase planes similar to the plane wave. The modes take ultrahigh Q factors as the field patterns are well confined in the transverse direction with near zero radiation loss at the vertices, and the narrow transverse mode field patterns result in large transverse mode intervals. In contrast, the main transverse mode field patterns in Fig. 4(c) are well focused by the circular sides as concave mirrors with the narrowest main beam width at the diagonals, but strong focused effect causes additional field beams with a large radiation loss. Therefore the ultrahigh Q modes exist as the deformation magnitudes are smaller and larger than the strong focused case.

In comparison, we obtain a Q factor of 1.5×10^4 for the high Q coupled mode at 1564.8 nm in a similar size circular resonator with a radius of $8 \mu\text{m}$ connecting a $1.5\text{-}\mu\text{m}$ -wide waveguide. For the CSR with each vertex connecting a $1.5\text{-}\mu\text{m}$ -wide output waveguide, the fundamental transverse mode at 1547.4 nm can still have an ultrahigh Q factor of 1.5×10^{11} as $a = 16 \mu\text{m}$ and $\delta = 1.4 \mu\text{m}$. The CSRs with ultrahigh Q modes can be a versatile element for photonic integrated circuits. Ultrahigh Q modes can also exist in deformed circular microcavities with the coexistence of regular and chaotic ray dynamics for channeling chaotic rays into the output waveguide [21]. However, the mode field distributions in the square resonators have special behaviors for guaranteeing stable and controllable dual-mode lasing as discussed in the following.

Then we demonstrate the stability of dual-mode lasing for square resonator microlasers based on nonlinear gain analysis of density matrix formalism [38]. Accounting the nonlinear

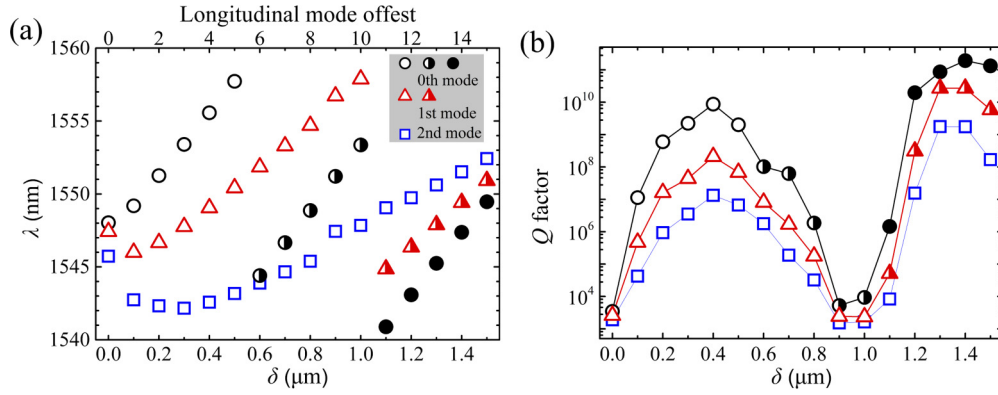


FIG. 3. (a) Resonance wavelengths around 1550 nm and (b) corresponding mode Q factors versus the deformation amplitude δ . The zeroth-, first-, and second-order transverse modes are marked by circle, triangle, and square symbols, respectively. The variation of the longitudinal mode number is also traced in (a) for the square marked modes. The open, half-filled, and solid symbols belong to different longitudinal modes at the same value of δ .

gain, the mode gain G_m of mode m can be expressed as

$$G_m = g_m - \sum_k G_{m(k)} S_k. \quad (1)$$

where g_m is the first-order gain coefficient and S_k is the photon density of mode k . The third-order gain coefficient $G_{m(k)}$ is related to the overlap between the intensity of the mode m and the spatial distribution of the carrier hole burning caused by the mode k as

$$G_{m(k)} = \frac{c}{1 + \delta_{m,k}} \int |F_m(r) F_k(r)|^2 dr, \quad (2)$$

where $F_m(r)$ and $F_k(r)$ are the field distributions of modes m and k , c is a constant proportional to the linear gain and relates to carrier intraband relaxation times, and $1/(1 + \delta_{m,k})$ comes from the numbers of field component combinations in squared electric field. Based on dual-mode rate equation analysis, the dual-mode stationary solution is stable if and only if the cross-saturation coefficient is smaller than the self-saturation coefficient, i.e., the ratio of $G_{m(k)}/G_{k(k)} < 1 (m \neq k)$ [32]. For two longitudinal modes with the same transverse mode number in a Fabry-Perot cavity, the ratio is 4/3 [38], so the other

mechanism should be provided to realize dual-mode stable operation. For example, quantum dot semiconductor lasers were proposed to avoid the inevitable mode competition in the bulk or quantum well semiconductor lasers [32]. However, two modes with totally different transverse mode and longitudinal mode numbers can satisfy the stable condition of dual-mode stationary solution, because of the weak overlap between the intensity distributions of the two modes with the ratio $G_{m(k)}/G_{k(k)}$ of 8/9 [38]. In the square resonator, the mode field patterns are determined by the mode numbers p and q of wave node numbers along the directions of the square sides instead of the longitudinal and transverse mode numbers [21,30]. The nearby high Q confined modes usually have totally different values of p and q , even if they have the same longitudinal mode number or transverse mode number. For example, the fundamental and the first-order transverse modes with the same longitudinal mode number will have the mode numbers of $(p, p + 2)$ and $(p - 1, p + 3)$, so the ratio of the cross-saturation coefficient to the self-saturation coefficient should satisfy the stable condition of dual-mode stationary solution. For the CSRs, the ultrahigh Q modes with mode field patterns in Figs. 4(b) and 4(d) are mainly determined by

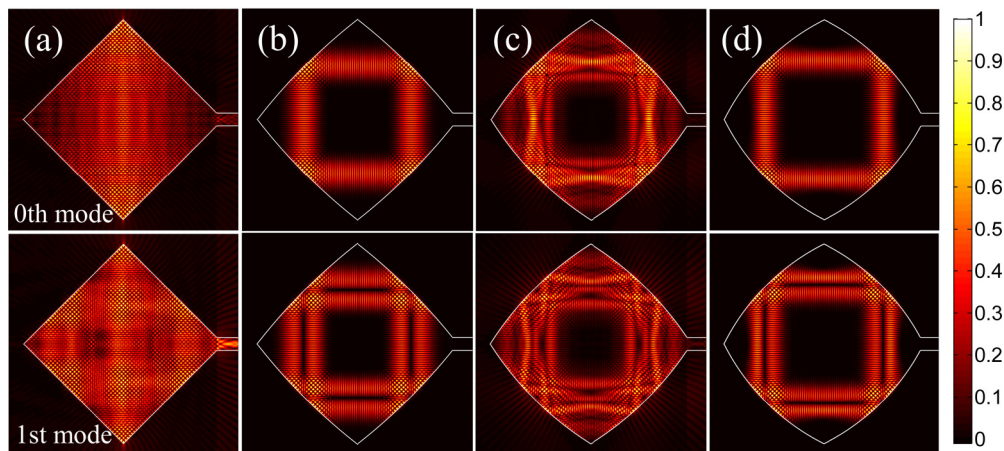


FIG. 4. (a)–(d) The distributions of $|H_z|$ for the zeroth (upper) and first (lower) symmetric transverse modes as $\delta = 0, 0.5, 0.9,$ and $1.3 \mu\text{m}$, respectively.

TABLE I. The ratio of cross-saturation coefficient to self-saturation coefficient.

δ (μm)	0	0.5	1.1	1.3	1.5
$G_{0(1)}/G_{0(0)}$	0.95	0.90	0.64	0.66	0.67
$G_{0(1)}/G_{1(1)}$	0.95	1.08	0.83	0.82	0.82

the longitudinal and transverse mode numbers again, instead of the aforementioned mode numbers p and q . From Fig. 3(a), we can find that the nearby fundamental and first-order transverse modes belong to different longitudinal mode numbers as $\delta > 0.6 \mu\text{m}$, due to the enhancement of the transverse mode interval. So they should satisfy the dual-mode lasing stability condition. Based on Eq. (2), we calculate $G_{m(k)}/G_{k(k)}$ for nearby ultrahigh Q modes at $\delta = 0, 0.5, 1.1, 1.3,$ and $1.5 \mu\text{m}$ and summarize the results in Table I, where the subscripts “0” and “1” indicate the fundamental and first-order transverse modes, respectively. The ratios are smaller than 1 at $\delta = 1.1, 1.3,$ and $1.5 \mu\text{m}$ because the nearby high Q modes have totally different mode numbers. But the selected modes at $\delta = 0.5 \mu\text{m}$ belong to the same longitudinal mode, so the coefficient of $G_{0(1)}/G_{1(1)}$ is larger than 1. Therefore stable dual-mode lasing can be expected for the CSR microlasers by choosing a suitable deformation value.

III. LASING SPECTRUM AND AUTOCORRELATION MEASUREMENTS

The square microlasers with a vertex output waveguide are fabricated using an AlGaInAs/InP laser wafer with eight pairs of compressively strained multiple quantum wells [28]. The quantum wells and barrier layers with thickness of about 6 and 9 nm are sandwiched between two 90-nm AlGaInAs separate confinement layers. The upper confinement layers are

1.2- μm p -InP and 0.1- μm p^+ -InGaAs contacting layer. The square resonator patterns are transferred onto the SiO_2 layer using contacting photolithography and inductively coupled plasma (ICP) etching techniques, and the laser wafer is etched to about 4.5 μm using the ICP technique again with the patterned SiO_2 layer as a hard mask. The side-view scanning electron microscope (SEM) image after inductively coupled plasma (ICP) etching is shown in the inset of Fig. 5(b), and the top-view microscope image of a microlaser is shown in the inset of Fig. 5(c). The fabricated devices are tested at the temperature of 288 K by butt-coupling a fiber to the cleaving facet of the output waveguide. Lasing spectra for the CSR microlasers are plotted in Figs. 5(a)–5(f) at $\delta = 0, 0.5, 0.9, 1.1, 1.3,$ and $1.5 \mu\text{m}$, respectively. By comparing the numerical results, the fundamental, first-, second-, and third-order transverse modes are assigned and marked by the circle, triangle, square, and pentagram symbols, respectively, as in Fig. 3. Dual-mode lasing with the wavelength intervals of 5.98, 3.43, 2.46, and 1.26 nm are obtained at $\delta = 0.5, 1.1, 1.3,$ and $1.5 \mu\text{m}$, and near dual-mode lasing with an intensity ratio of 7.9 dB is observed at $\delta = 0$. Single-mode lasing at 1555 nm with the side-mode-suppression ratio (SMSR) of 33 dB is obtained for the CSR laser with $\delta = 0.9 \mu\text{m}$ at 35 mA due to the low Q factor as shown in Fig. 3(b). A pair of four-wave mixing peaks is clearly exhibited in the lasing spectra in Fig. 5(a), which indicates the coexistence of the dual-mode lasing. The results indicate that the CSRs with ultrahigh Q modes easily realize dual-mode lasing and the transverse mode interval can be adjusted by varying the radius of the circular sides. More resonant peaks appear in Figs. 5(e) and 5(f) corresponding to the ultrahigh Q factors, because more higher-order transverse modes also have large Q factors. The mode linewidths are estimated by fitting the lasing spectra at about threshold current with Lorentz curves.

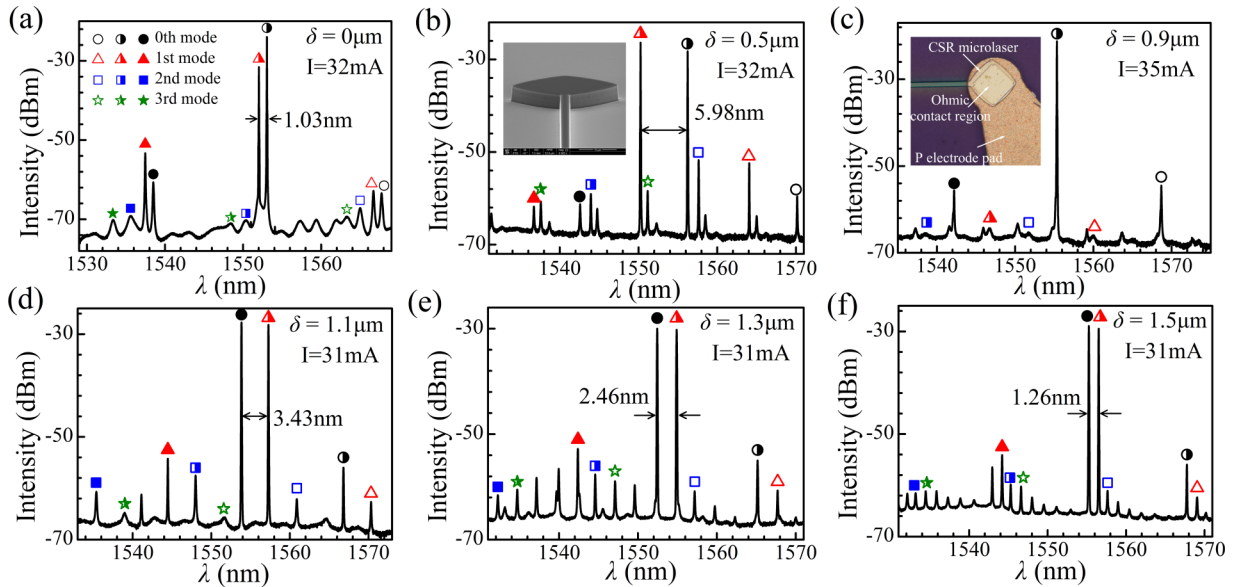


FIG. 5. (a)–(f) Lasing spectra for the CSR lasers with $a = 16$ and $w = 1.5$ at δ of 0.5, 0.7, 0.9, 1.1, 1.3, and $1.5 \mu\text{m}$, respectively. The zeroth- first-, second-, and third-order transverse modes are marked by circle, triangle, square, and pentagram symbols, respectively, with the open, half-filled, and solid symbols belonging to different longitudinal modes. Insets in (b),(c) are a side-view SEM image after ICP etching and a top-view microscope image of a microlaser.

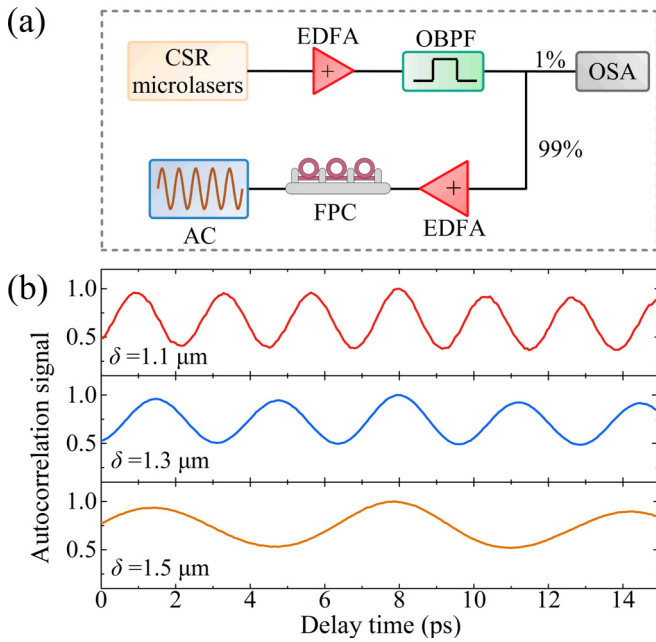


FIG. 6. Autocorrelation measurements based on the dual-mode CSR microlasers. (a) Experimental setup. (b) Measured autocorrelation pulse trains for the lasers with δ of 1.1, 1.3, and 1.5 μm , respectively. EDFA = erbium-doped fiber amplifier; OBPF = optical bandpass filter; OSA = optical spectral analyzer; FPC = fiber polarization controller; AC = autocorrelator.

The linewidths of the zeroth and the first modes are limited by the resolution of 0.02 nm, while the values of 0.14, 0.1, and 0.11 nm are obtained for the second modes, and 0.85, 0.15, and 0.13 nm for the third modes, as $\delta = 1.1, 1.3$, and 1.5 μm , respectively. The transverse mode intervals $\Delta\lambda_{01}$, $\Delta\lambda_{02}$, and $\Delta\lambda_{03}$ are varied with δ at the rates of 5.2, 10.2, and 14.9 nm/ μm for the CSR lasers as $0.5 \leq \delta \leq 1.5 \mu\text{m}$, which are in good agreement with the numerical results of 5.2, 9.8, and 14.1 nm/ μm .

Finally, we demonstrate the potential generation of THz beating signals from the CSR lasers by using the noncollinear intensity autocorrelator [39,40]. As is shown in Fig. 6(a), the dual-mode output signal of the CSR microlaser is preamplified by an erbium-doped fiber amplifier (EDFA). Then the amplified output is filtered by a tunable optical bandpass filter (OBPF), and split up into two parts with 1% of the light for monitoring the optical spectra; 99% of the light

is amplified and injected to the autocorrelator to detect the beating frequency after the fiber polarization controller (FPC). Autocorrelation pulse trains are plotted in Fig. 6(b) for the CSR lasers operated at 31 mA. The sinusoidal modulation signals of the pulse trains have the average periods of 2.34, 3.22, and 6.44 ps as $\delta = 1.1, 1.3$, and 1.5 μm , respectively, corresponding to the beating frequencies of 0.43, 0.31, and 0.16 THz. The results also indicate the coexistence of dual-mode stable operation for the CSR microlasers.

IV. DISCUSSIONS AND CONCLUSIONS

The CSR microlasers with high Q factors can support stable dual-mode lasing. However, ultrahigh passive mode Q factors will limit the output coupling efficiency of the waveguide when considering the material absorption loss. To increase the output coupling efficiency, the mode Q factors can be compromised by designing an output waveguide parallel to mode light ray, i.e., rotating the output waveguide in Fig. 1 by 90° . The width of the waveguide and the opening window of the resonator to the waveguide can be adjusted for intercepting the diffused rays and realizing high-efficiency output to the attached waveguide, but still keeping high Q factors for dual-mode lasing. The circular-side square microresonators with ultrahigh Q factors provide plenty of space to adjust the mode Q factor for improving the output efficiency.

In summary, we have designed and demonstrated circular-side square resonator microlasers with enhanced mode Q factors and transverse mode intervals. Stable dual-transverse-mode lasing AlGaInAs/InP microlasers are realized with frequency intervals ranging from 160 to 430 GHz benefitting from the side deformation. We expect that dual-mode lasing circular-side square resonator microlasers can be applied to generate sub-THz waves for high-capacity THz wireless communications. The high Q circular-side square microresonator will be a versatile microresonator in photonic integrated circuits for optical signal processing, optical delay, and storage.

ACKNOWLEDGMENTS

This work was supported by the National Natural Science Foundation of China under Grants No. 61235004, No. 61527823, and No. 61377105. The authors would like to thank Professor Qinghai Song for discussions and suggestions about light ray simulation.

- [1] K. J. Vahala, *Nature* **424**, 839 (2003).
- [2] L. He, Ş. K. Özdemir, and L. Yang, *Laser Photon. Rev.* **7**, 60 (2013).
- [3] M. T. Hill and M. C. Gather, *Nat. Photon.* **8**, 908 (2014).
- [4] X. M. Lv, Y. Z. Huang, L. X. Zou, H. Long, and Y. Du, *Laser Photon. Rev.* **7**, 818 (2013).
- [5] X. F. Jiang, C. L. Zou, L. Wang, Q. H. Gong, and Y. F. Xiao, *Laser Photon. Rev.* **10**, 40 (2016).
- [6] J. U. Nöckel and A. D. Stone, *Nature* **385**, 45 (1997).
- [7] C. Gmachl, F. Capasso, E. Narimanov, J. U. Nöckel, A. D. Stone, J. Faist, D. L. Sivco, and A. Y. Cho, *Science* **280**, 1556 (1998).
- [8] S. B. Lee, J. H. Lee, J. S. Chang, H. J. Moon, S. W. Kim, and K. An, *Phys. Rev. Lett.* **88**, 033903 (2002).
- [9] S. K. Kim, S. H. Kim, G. H. Kim, H. G. Park, D. J. Shin, and Y. H. Lee, *Appl. Phys. Lett.* **84**, 861 (2004).
- [10] G. Chern, H. Tureci, A. D. Stone, R. Chang, M. Kneissl, and N. Johnson, *Appl. Phys. Lett.* **83**, 1710 (2003).
- [11] C. M. Kim, J. Cho, J. Lee, S. Rim, S. H. Lee, K. R. Oh, and J. H. Kim, *Appl. Phys. Lett.* **92**, 131110 (2008).
- [12] M. Kraft and J. Wiersig, *Phys. Rev. A* **89**, 023819 (2014).
- [13] J. Wiersig and M. Hentschel, *Phys. Rev. Lett.* **100**, 033901 (2008).

- [14] R. Dubertrand, E. Bogomolny, N. Djellali, M. Lebental, and C. Schmit, *Phys. Rev. A* **77**, 013804 (2008).
- [15] Q. H. Song, L. Ge, A. D. Stone, H. Cao, J. Wiersig, J. B. Shim, J. Unterhinninghofen, W. Fang, and G. S. Solomon, *Phys. Rev. Lett.* **105**, 103902 (2010).
- [16] X. F. Jiang, Y. F. Xiao, C. L. Zou, L. He, C. H. Dong, B. B. Li, Y. Li, F. W. Sun, L. Yang, and Q. Gong, *Adv. Mater.* **24**, OP260 (2012).
- [17] S. V. Boriskina, T. M. Benson, P. Sewell, and A. I. Nosich, *IEEE J. Sel. Top. Quantum Electron.* **12**, 52 (2006).
- [18] C. P. Dettmann, G. V. Morozov, M. Sieber, and H. Waalkens, *Phys. Rev. A* **80**, 063813 (2009).
- [19] Q. J. Wang, C. Yan, N. Yu, J. Unterhinninghofen, J. Wiersig, C. Pflügl, L. Diehl, T. Edamura, M. Yamanishi, and H. Kan, *Proc. Natl. Acad. Sci. USA* **107**, 22407 (2010).
- [20] S. S. Sui, Y. Z. Huang, M. Y. Tang, H. Z. Weng, Y. D. Yang, J. L. Xiao, and Y. Du, *Opt. Lett.* **41**, 3928 (2016).
- [21] Q. H. Song, L. Ge, B. Redding, and H. Cao, *Phys. Rev. Lett.* **108**, 243902 (2012).
- [22] W. H. Guo, Y. Z. Huang, Q. Y. Lu, and L. J. Yu, *IEEE J. Quantum Electron.* **39**, 1106 (2003).
- [23] Y. D. Yang and Y. Z. Huang, *IEEE J. Quantum Electron.* **43**, 497 (2007).
- [24] Y. D. Yang and Y. Z. Huang, *Phys. Rev. A* **76**, 023822 (2007).
- [25] S. V. Boriskina, T. M. Benson, P. Sewell, and A. I. Nosich, *IEEE J. Quantum Electron.* **41**, 857 (2005).
- [26] H. J. Moon, K. An, and J. H. Lee, *Appl. Phys. Lett.* **82**, 2963 (2003).
- [27] H. Long, Y. Z. Huang, X. W. Ma, Y. D. Yang, J. L. Xiao, L. X. Zou, and B. W. Liu, *Opt. Lett.* **40**, 3548 (2015).
- [28] M. Y. Tang, S. S. Sui, Y. D. Yang, J. L. Xiao, Y. Du, and Y. Z. Huang, *Opt. Express* **23**, 27739 (2015).
- [29] P. Panindre and S. Kumar, *Opt. Lett.* **41**, 878 (2016).
- [30] S. Bittner, C. Lafargue, I. Gozhyk, N. Djellali, L. Milliet, D. Hickox-Young, C. Ulysse, D. Bouche, R. Dubertrand, and E. Bogomolny, *Europhys. Lett.* **113**, 54002 (2016).
- [31] Y. D. Yang and Y. Z. Huang, *J. Phys. D: Appl. Phys.* **49**, 253001 (2016).
- [32] L. Chusseau, F. Philippe, P. Viktorovitch, and X. Letartre, *Phys. Rev. A* **88**, 015803 (2013).
- [33] T. Nagatsuma, G. Ducournau, and C. C. Renaud, *Nat. Photon.* **10**, 371 (2016).
- [34] S. Koenig, D. Lopez-Diaz, J. Antes, F. Boes, R. Henneberger, A. Leuther, A. Tessmann, R. Schmogrow, D. Hillerkuss, and R. Palmer, *Nat. Photon.* **7**, 977 (2013).
- [35] A. C. Sodre, J. C. Boggio, A. Rieznik, H. Hernandez-Figueroa, H. Fragnito, and J. Knight, *Opt. Express* **16**, 2816 (2008).
- [36] E. Myslivets, B. P. Kuo, N. Alic, and S. Radic, *Opt. Express* **20**, 3331 (2012).
- [37] H. Z. Weng, Y. Z. Huang, J. L. Xiao, Y. D. Yang, X. W. Ma, F. L. Wang, and Y. Du, *Opt. Lett.* **41**, 5146 (2016).
- [38] M. Yamada, *IEEE J. Quantum Electron.* **19**, 1365 (1983).
- [39] M. Uemukai, H. Ishida, A. Ito, T. Suhara, H. Kitajima, A. Watanabe, and H. Kan, *Jpn. J. Appl. Phys.* **51**, 020205 (2012).
- [40] N. Kim, J. Shin, E. Sim, C. W. Lee, D. S. Yee, M. Y. Jeon, Y. Jang, and K. H. Park, *Opt. Express* **17**, 13851 (2009).